

# Unsaturated Wet Granular Materials Rheology: A Study Using X-ray Micro-tomography and Deep Learning Models

Abdoulaye Fall<sup>1,\*</sup>, Ahmad Awdi<sup>1</sup>, Camille Chateau<sup>1</sup>, and Jean-Noel Roux<sup>1</sup>

<sup>1</sup>Laboratoire Navier, Université Gustave-Eiffel, ENPC, CNRS, Champs sur Marne, France.

**Abstract.** This study presents experiments and discrete element simulations of simple, normal stress-controlled shear flows in model unsaturated granular materials, consisting of frictional spheres bonded by a small amount of wetting liquid. The rheology is characterized by the internal friction coefficient  $\mu_w^*$  and solid fraction  $\phi_s$ , as functions of reduced pressure  $P^*$  and a visco-inertial number  $J = I_v + 2I^2$ . X-ray micro-tomography is used to explore the microstructure, with advanced segmentation techniques combining Random Forest and U-Net models for accurate phase distinction and quantification. A new automated tool classifies liquid morphologies, demonstrating shear-induced redistribution and clustering. Coordination number estimation further details interactions between solid particles and liquid phases, providing a robust methodology for quantitative analysis of wet granular material microstructures.

## 1 Introduction

Unsaturated wet granular materials, composed of solid particles, liquid phases, and voids, exhibit complex microstructures crucial for geotechnical and environmental applications. Their flow behavior is governed by liquid wetting, which induces cohesion via surface tension [1–3]. These materials transition through pendular, funicular, capillary, and slurry states based on liquid content [4]. The interplay of capillary and viscous forces significantly influences their mechanics and shear behavior [5, 6].

Classical granular rheology has been extended to include liquid viscosity, with the macroscopic friction coefficient  $\mu_w^*$  and solid fraction  $\phi_s$  governed by the visco-inertial number  $J$ , capturing inertial and viscous effects [7–10]. The reduced pressure  $P^*$  further characterizes these materials by comparing confining force to meniscus tensile strength [2].

Microstructural characterization is essential for understanding wet granular mechanics. X-ray micro-tomography enables three-dimensional quantification of phase distribution, liquid morphology, and contact networks [11–13]. This work demonstrates that shear deformation induces liquid redistribution, clustering, and changes in coordination number, affecting mechanical response. We establish a robust methodology for quantitative analysis of wet granular material microstructures, combining experiments, simulations, and advanced segmentation techniques.

## 2 Experimental and Numerical Methods

Experiments were conducted using a custom annular shear cell (Figure 1a) designed to study granular rheology un-

der controlled pressure [14]. A stress-controlled rheometer (Anton Paar MCR 502) applied shear, while an X-ray micro-tomography setup [9] enabled real-time imaging of microstructural evolution, capturing liquid redistribution and contact network changes (Figure 1b). The sample consisted of frictional polystyrene beads ( $d = 0.58$  mm) mixed with silicone oil, varying in viscosity and liquid fraction. Details of the experimental procedures can be found in [9, 15].

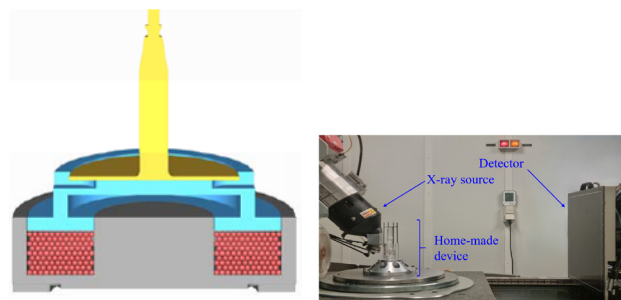


**Figure 1.** Cross-section of the annular shear flow: shear and pressure are applied via a rotating ring on the rheometer, which moves vertically under imposed shear rate and pressure. (b) X-ray imaging setup at Navier, with the rotation and centering system positioned beneath the tomograph stage.

The numerical model simulates wet granular materials under shear, using DEM with Hertzian contact elasticity and friction [8]. Capillary forces in the pendular regime are modeled using the Maugis approximation, and viscous forces are incorporated via the lubrication approximation [8, 15]. Simulations are conducted for various reduced pressures and viscosities (see [8, 15] for details).

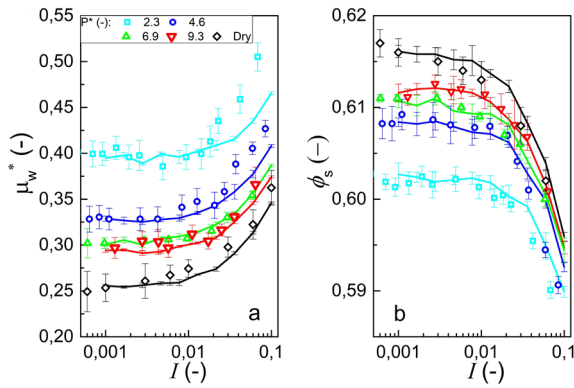
\*e-mail: [abdoulaye.fall@univ-eiffel.fr](mailto:abdoulaye.fall@univ-eiffel.fr)

Advanced image segmentation techniques, combining Random Forest and U-Net models, were used to extract quantitative microstructural information.

### 3 Results and Discussion

#### 3.1 Macroscopic Rheology

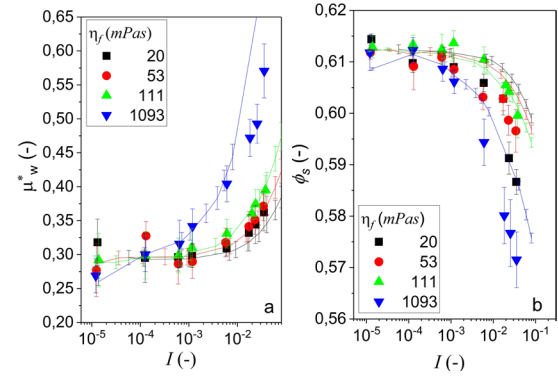
The rheology follows a friction law involving the inertial number  $I$  and reduced pressure  $P^*$ , which compares confinement stress to cohesive stress. The friction law remains non-singular in the quasistatic and cohesive limits. Measurements in Figure 2 show that the effective friction coefficient  $\mu^*$  increases as  $P^*$  decreases, demonstrating the role of capillary forces in enhancing shear resistance.



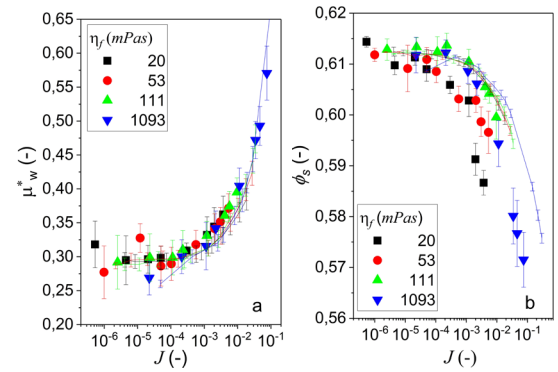
**Figure 2.** Experimental results for the macroscopic friction coefficient  $\mu_w^*$  (a) and solid fraction  $\phi_s$  (b) versus inertial number  $I$  for different values of reduced pressure  $P^*$  for  $\epsilon = 0.03$  and  $\eta_f = 20mPas$ . Data from [9].

Figure 3 shows how increasing liquid viscosity affects the friction coefficient  $\mu_w^*$  and solid fraction  $\phi_s$  at fixed  $P^*$ . For  $\eta_f > 0.1$  Pa s, viscous effects significantly enhance shear strength and dilation. As the system transitions from inertial to viscosity-dominated behavior, the visco-inertial number  $J = I_v + 2I^2$ , incorporating  $I_v = \eta_f \dot{\gamma} / \sigma_n$  and  $I$ , better captures both capillary and viscous contributions. The principle of stress additivity underpins the concept of  $J$ , suggesting that the total stress in a granular material can be expressed as a linear combination of individual stress components, such as inertial, viscous, and cohesive stresses [10]. In our study, cohesive stress is implicitly considered within the reduced pressure  $P^*$ , rather than being explicitly accounted for separately.

Figure 4 illustrates the use of the visco-inertial number  $J$  for  $P^* = 9.3$ , comparing experimental and numerical data. The graphs reveal that while both the friction coefficient  $\mu_w^*$  and solid fraction  $\phi_s$  exhibit trends with respect to the visco-inertial number  $J$ , there are more noticeable discrepancies in the case of the solid fraction. Specifically, as the visco-inertial number increases, the friction coefficient increases, particularly for higher viscosities, and the DEM results align closely with experimental observations.



**Figure 3.** Experimental (symbols) and simulation (lines) results of the friction coefficient  $\mu_w^*$  (a) and solid fraction  $\phi_s$  (b) versus inertial number  $I$  for a reduced pressure  $P^* = 9.3$  and for different viscosity values of the wetting liquid.



**Figure 4.** Friction coefficient (a) and solid fraction (b) versus the visco-inertial number  $J$  for a reduced pressure of  $P^* = 9.3$  and for different viscosity values of the wetting liquid. The lines are the DEM results.

However, for the solid fraction, although both experimental data and DEM results show a decrease with increasing visco-inertial number, the discrepancies are more pronounced. This discrepancy likely arises from challenges in maintaining sample homogeneity and achieving high experimental reproducibility in grain-liquid mixtures.

#### 3.2 Segmentation Method

The raw X-ray tomography images as shown in Fig.5a reveal a three-phase system composed of solid grains, liquid, and voids. Identifying and quantifying these phases is essential for understanding how shear affects phase distribution and overall material behavior.

To accurately differentiate between solid, liquid, and void phases in X-ray tomography images, we employ an artificial-intelligence-based segmentation approach. Our method integrates a Random Forest classifier and a U-Net convolutional neural network, leveraging their combined strengths for robust phase identification. The Random Forest model is trained on manually labeled datasets, learning statistical features such as intensity gradients and texture variations. The U-Net model further refines segmentation

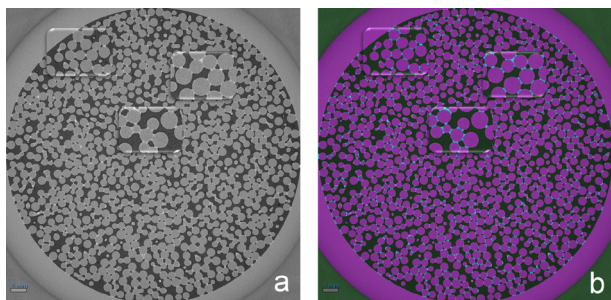


**Figure 5.** Horizontal slice from the 3D image,  $8\mu\text{m}$  voxel size a) before segmentation b) after segmentation with the trained 2D U-net model. The air, polystyrene beads, and silicone oil are colored green, violet, and cyan respectively.

by incorporating spatial context, improving boundary detection and minimizing classification errors. An example of segmentation result is presented in Fig.5b.

Fig. 6 shows several typical liquid morphologies extracted from the segmented images, illustrating the diverse forms that liquid structures can take within the granular material. One of the key objectives of this study is to distinguish between these morphologies and to track how they evolve under shear load.

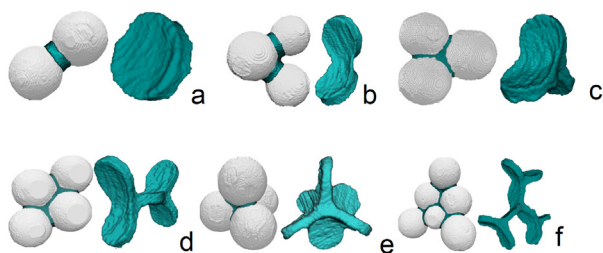


**Figure 6.** Extracted liquid morphologies from the sample after segmentation a) Liquid or capillary bridge (cb): two neighboring grains in contact, b) Dimer (di), and c) Trimer (tr): three neighboring grains in contact, d) Pentamer (pt), and e) Tetrahedral (th): four neighboring grains in contact, and f) others: big liquid morphology with five or more neighboring grains in contact.

Additionally, we implement an automated classification algorithm to identify liquid morphologies using geometric and topological descriptors. The algorithm distinguishes capillary bridges, trimers, and larger clusters, capturing shear-induced coalescence and the formation of elongated or percolating structures as shown in Fig.7.

This segmentation pipeline enables precise quantification of phase fractions and local structural changes. By applying it to sheared samples, we extract valuable metrics such as the evolution of liquid cluster sizes, particle coordination numbers, and contact network topologies. The automated nature of this approach ensures reproducibility and scalability, making it applicable to a wide range of granular systems with varying levels of saturation and particle size distributions.

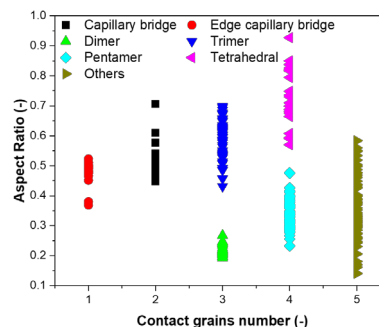


**Figure 7.** The aspect ratio versus the number of contact of each liquid morphologies. Edge capillary bridges are the capillary bridges formed between one grain and the edge of the sample container.

### 3.3 Microstructure Evolution

Figure 8 shows the liquid volume distribution among different morphology types. At low liquid content  $\epsilon = 0.05$ , as shown in Fig. 8a, with samples at  $\epsilon = 0.03$  exhibiting the same trend), capillary bridges dominate, though their share decreases from 85% to 70% under shear.

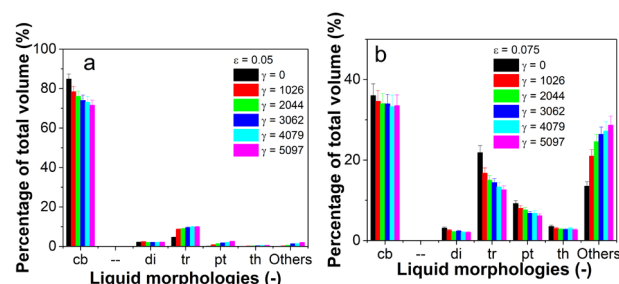


**Figure 8.** Proportion of the total liquid volume occupied by each morphology type at different liquid contents: a)  $\epsilon = 0.05$  and b)  $\epsilon = 0.075$ .

At higher liquid content ( $\epsilon = 0.075$  as shown in Fig.8b), smaller morphologies (dimers, trimers, tetrahedrals, pentamers) decrease in volume, while larger clusters ('others') grow, indicating shear-induced coalescence of liquid structures.

The biggest percolating liquid morphologies found at  $\gamma = 5097$  are shown in Figure 9. These large liquid clusters are formed of trimers, pentamers, and tetrahedrals cluster units, forming a branched open structure [16] especially for the largest liquid content  $\epsilon = 0.075$ .

Figure 10 presents the radial distribution function (RDF)  $g(r)$  for  $\epsilon = 0.03$  at different deformations  $\gamma$ . The RDF, which describes particle density variations relative to a reference particle [17, 18], maintains a consistent profile across all liquid contents. This stability reflects the quasistatic regime of the X-ray micro-tomography experiments ( $I \leq 10^{-3}$ ), where slow deformation preserves the overall particle structure.

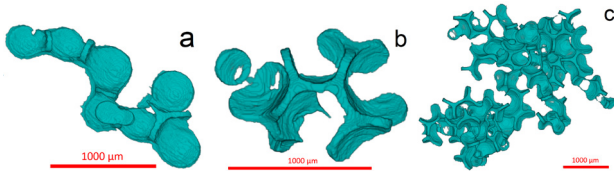


**Figure 9.** The largest percolating liquid cluster extracted from the X-ray micro-tomography images at a liquid contents of a)  $\epsilon = 0.03$ , b)  $\epsilon = 0.05$ , and c)  $\epsilon = 0.075$  for shear deformation  $\gamma = 5097$ .

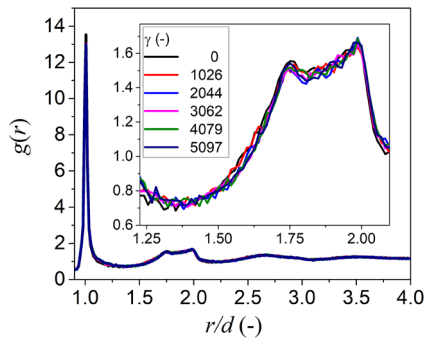


**Figure 10.** The radial distribution function profile with shear deformation  $\gamma$  in sample with liquid content of  $\epsilon = 0.03$ . The  $\epsilon = 0.05$  and  $\epsilon = 0.075$  samples show the same trend. The inset is a zoom-in to show the peak shapes for  $r/d$  between  $r = \sqrt{3}$  and  $r = 2$ .

The coordination number  $Z$ , or average interactions per particle, is given by  $Z = Z_C + Z_D$  [8], where  $Z_C$  represents contact interactions and  $Z_D$  accounts for distant interactions via liquid bridges.

The contact coordination number  $Z_C$  is estimated using the RDF:

$$Z_C = 4\pi\rho \int_{r_i}^{r_0} g(r)r^2 dr, \quad (1)$$

where  $\rho$  is the grain number density, and  $r_i = 0.95d$ ,  $r_0 = 1.05d$  are bounds near the particle diameter  $d$ . This yields  $Z_C \approx 5.5$ , in agreement with simulations [8].

In the pendular regime, capillary bridges dominate. The distant coordination number  $Z_D$  is obtained by normalizing the number of capillary bridges (excluding edge effects) by the grain count  $N_g$  and subtracting  $Z_C$ . Without shear,  $Z_D \approx 3.2$ , consistent with simulations [8]. Under shear,  $Z_D$  drops to  $\sim 2.75$  due to dilation, increasing grain spacing and reducing capillary bridges.

The velocity profile (Figure 11) shows the distribution of shear rates across the sample. The shear rate is non-zero primarily between 3.75 and 9.6 mm in the  $z$ -direction.

The highest shear rate regions align with the most significant morphological changes in the heat maps. Shear redistributes liquid morphologies, with capillary bridges remaining stable while dimers, trimers, and pentamers form locally. This underscores shear's key role in shaping liq-

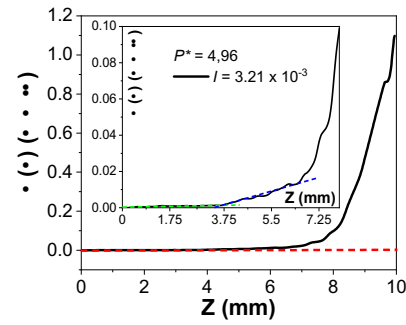


**Figure 11.** Vertical velocity profile for a sample with liquid content  $\epsilon = 0.03$ . The inertial number is  $I = 3.21 \times 10^{-3}$  and reduced pressure  $P^* = 4.96$ . The profile shows the distribution of shear rates across the sample, with the shear rate being non-zero primarily between 3.75 and 9.6 mm in the  $z$ -direction.

uid structures and the mechanics of unsaturated granular materials.

Figures 12 show the heat maps that illustrate the evolution of liquid morphologies under shear at  $\epsilon = 0.05$ . Capillary bridges (CB) dominate, with high-frequency zones marking concentrated regions. Dimers and trimers appear in localized areas, while pentamers are rare and form under specific conditions. At  $\epsilon = 0.075$  (data not shown), liquid distribution becomes more diffuse, with larger clusters forming and evolving under shear.

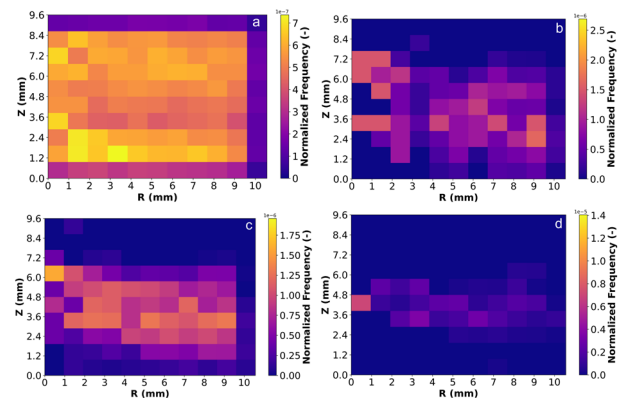


**Figure 12.** 2D heatmaps of the normalized frequencies after 8 min of shear ( $\gamma = 1.02 \times 10^3$ ) showing the distribution of: (a) Capillary bridges, (b) Dimers, (c) Trimers, and (d) Pentamers for  $\epsilon = 0.05$ . The heatmaps highlight the spatial distribution and prevalence of each morphology under shear. The normalized frequency is calculated by dividing the number of data points within each  $(r, z)$  zone by the product of the zone annular area, the total number of points in the dataset, and the corresponding liquid content.

## 4 Conclusion

This study explores the rheology and microstructure of unsaturated granular materials under shear through experiments and simulations. The macroscopic rheology ( $\mu_w^*$ ,  $\phi_s$ )

aligns well with simulations, governed by the visco-inertial number  $J$ . An AI-based segmentation method quantifies liquid and solid fractions, revealing how shear influences microstructural evolution. Heat maps highlight capillary bridges as stable, while dimers, trimers, and larger clusters form in high-shear regions. Velocity profiles confirm that shear drives liquid redistribution, linking microscopic rearrangements to macroscopic behavior. Future work will refine these correlations and extend the methodology to broader deformation regimes.

## References

- [1] R. Mani, D. Kadau, H.J. Herrmann, Liquid migration in sheared unsaturated granular media, *Granular Matter* **15**, 447 (2013).
- [2] S. Khamseh, J.N. Roux, F. Chevoir, Flow of wet granular materials: A numerical study, *Physical Review E* **92**, 022201 (2015).
- [3] M. Scheel, R. Seemann, M. Brinkmann, M. Di Michiel, A. Sheppard, B. Breidenbach, S. Herminghaus, Morphological clues to wet granular pile stability, *Nature materials* **7**, 189 (2008).
- [4] N. Mitarai, H. Nakanishi, Simple model for wet granular materials with liquid clusters, *EPL (Europhysics Letters)* **88**, 64001 (2010).
- [5] M. Pakpour, M. Habibi, P. Møller, D. Bonn, How to construct the perfect sandcastle, *Scientific reports* **2**, 1 (2012).
- [6] S.M. Iveson, J.A. Beathe, N.W. Page, The dynamic strength of partially saturated powder compacts: the effect of liquid properties, *Powder Technology* **127**, 149 (2002).
- [7] A. Awdi, C. Chateau, F. Chevoir, J.N. Roux, A. Fall, Viscous dissipation in large amplitude oscillatory shear of unsaturated wet granular matter, *Journal of Rheology* **67**, 365 (2023).
- [8] M. Badetti, A. Fall, F. Chevoir, J.N. Roux, Shear strength of wet granular materials: macroscopic cohesion and effective stress – discrete numerical simulations, confronted to experimental measurements, *Eur. Phys. J. E* **41**, 68 (2018).
- [9] M. Badetti, A. Fall, D. Hautemayou, F. Chevoir, P. Aimedieu, S. Rodts, J.N. Roux, Rheology and microstructure of unsaturated granular materials: Experiments and simulations, *J. Rheol.* **1175**, 1175 (2018).
- [10] T.T. Vo, S. Nezamabadi, P. Mutabaruka, J.Y. Delenne, F. Radjai, Additive rheology of complex granular flows, *Nature communications* **11**, 1 (2020).
- [11] E. Andò, S.A. Hall, G.C. Viggiani, J. Desrues, P. Bésuelle, Experimental micromechanics: grain-scale observation of sand deformation, *Géotechnique Letters* **2**, 107 (2012). [10.1680/geolett.12.00027](https://doi.org/10.1680/geolett.12.00027)
- [12] M. Scheel, R. Seemann, M. Brinkmann, M. Di Michiel, A. Sheppard, S. Herminghaus, Liquid distribution and cohesion in wet granular assemblies beyond the capillary bridge regime, *J. Phys. Condens. Matter.* **20**, 494236 (2008).
- [13] C. Semperebon, M. Scheel, S. Herminghaus, R. Seemann, M. Brinkmann, Liquid morphologies and capillary forces between three spherical beads, *Phys. Rev. E* **94**, 012907 (2016). [10.1103/PhysRevE.94.012907](https://doi.org/10.1103/PhysRevE.94.012907)
- [14] A. Fall, G. Ovarlez, D. Hautemayou, C. Mézière, J.N. Roux, F. Chevoir, Dry granular flows: Rheological measurements of the  $\mu$  (i)-rheology, *Journal of rheology* **59**, 1065 (2015).
- [15] L. Amarsid, A. Awdi, A. Fall, J.N. Roux, F. Chevoir, Viscous effects in sheared unsaturated wet granular materials, *Journal of Rheology* **68**, 523 (2024).
- [16] M. Scheel, Ph.D. thesis, Georg-August-University Göttingen (2010), <https://doi.org/10.53846/goediss-2677>
- [17] S. Torquato, H.W. Haslach Jr, Random heterogeneous materials: microstructure and macroscopic properties, *Appl. Mech. Rev.* **55**, B62 (2002).
- [18] S. Torquato, T.M. Truskett, P.G. Debenedetti, Is random close packing of spheres well defined?, *Physical review letters* **84**, 2064 (2000).